Turbulence-induced Non-Monotonic Influence of Aerosols on Cloud Droplet Size Distribution

Yiqi Chen[1,2], Jingyi Chen[1], and Chunsong Lu[1]

[1]China Meteorological Administration Aerosol-Cloud and Precipitation Key Laboratory and Collaborative Innovation Center on Forecast and Evaluation of Meteorological Disasters (CIC-FEMD), Nanjing University of Information Science and Technology, Nanjing, China
[2]Department of Atmospheric and Oceanic Sciences, School of Physics, Peking University, Beijing, China

Corresponding author: Jingyi Chen (jingyi.jenna.chen@outlook.com), Chunsong Lu (luchunsong110@gmail.com)

Key points:

- Cloud droplet size distribution first narrows and then broadens with increasing aerosol loading in large eddy simulations.
- A minimal model is proposed to explain the non-monotonic dependence of cloud droplet spectral relative dispersion on aerosol loading.
- The results reconcile both non-turbulent and turbulent scenarios regarding relationships between relative dispersion and aerosol loading.

Abstract

Cloud droplet size distribution is essential for quantifying the roles of clouds in earth system, including cloud albedo, precipitation formation, and cloud lifetime. The response of cloud droplet spectral relative dispersion (ε) to aerosol number concentration (N_a) as well as the role of turbulence in this response are yet puzzling. This study uses large eddy simulation to examine the ε–N_a relationship and derives an expression for ε from a minimal model to elucidate this relationship. Our findings indicate that as N_a increases, ε initially decreases because aerosols weaken turbulence-induced broadening more than condensational narrowing. However, as N_a continues to rise, ε increases as aerosols weaken condensational narrowing more significantly than turbulence-induced broadening. These findings improve the understanding of the aerosol effects on cloud droplet size distribution and address the challenge of quantifying aerosol indirect effects considering turbulence, potentially leading to new cloud microphysics parameterizations.

1 Introduction

Aerosol-cloud interactions are a major source of uncertainty in estimating climate change (Seinfeld et al., 2016). The relationship between aerosol number concentration (N_a) and the width of cloud droplet size distribution (DSD) plays an important role in the evaluation of the aerosol indirect effect and precipitation simulation (e.g., Liu and Daum, 2002; Xie et al., 2011; Chandrakar et al., 2016, 2018a, 2018b; Yin et al., 2022). The droplet spectral relative dispersion (ε), defined as the ratio of the standard deviation of droplet radius (σ) to the mean droplet radius ($\bar{r}$), is a commonly used metric for the width of DSD as it explicitly appears in the parameterizations of droplet effective radius and autoconversion rate (e.g., Pontikis and Hicks, 1992; Liu et al., 2014).

The ε–N_a relationship has two types: intra-cloud and inter-cloud (Hu et al., 2021). The intra-cloud relationship, using data points within a single cloud, reveals how non-aerosol factors like local activation fraction and updraft velocity cause spatial variations in both ε and N_a (or proxied by cloud droplet number concentration, N_c). Whereas the inter-cloud relationship, which represents the influence of background N_a on cloud-mean ε, can be used in global climate models (GCMs) to parameterize ε based on N_a (Rotstayn and Liu, 2003, 2005; Peng and Lohmann 2003; Wang et al., 2020). However, observations on the inter-cloud ε–N_a relationship remain highly ambiguous, showing positive, negative, and negligible correlations between ε and N_a or N_c (Hu et al., 2021). To better parameterize ε based on N_a, theoretical and numerical studies are needed on the inter-cloud ε–N_a relationship.

The impacts of adiabatic condensational growth on ε are regime-dependent (Liu et al., 2014; Peng et al., 2007; Chen et al., 2016, 2018). In the aerosol-limited regime, ε is positively correlated with N_a due to "condensational narrowing", as small droplets grow faster than large ones according to the theory of diffusive condensational growth. This effect was well quantified by an analytical expression for ε in Liu et al. (2006) (L06 hereafter). Conversely, in the updraft-limited regime, ε is negatively correlated with N_a due to "condensational broadening", which results from pronounced curvature and solute effects on droplet condensation under the suppressed supersaturation in this regime (Chen et al., 2016, 2018).

To elucidate the broadening of observed DSDs compared to that produced by adiabatic cloud parcel theories, various mechanisms have been developed, including entrainment and mixing (Jensen and Baker, 1989; Andrejczuk et al., 2004; Kumar et al., 2012; Kumar et al., 2018; Kumar et al., 2021), stochastic condensation (e.g., Jeffery et al. 2007), and turbulence-enhanced collision (e.g., Grabowski and Wang, 2013). Previous large eddy simulation (LES) studies (Igel and van den Heever, 2017; Wang et al., 2011) found that the ε–N_a correlation when considering clouds' cores is different from that correlation when considering entire clouds, which indicates that the ε–N_a relationships are influenced by entrainment and mixing. Chamber experiments and relevant LES simulations conducted by Chandrakar et al. (2016) and Thomas et al. (2019) found that ε is negatively correlated with N_a under turbulent conditions, which can be explained by an analytical expression for ε derived from the stochastic condensation theory (Chandrakar et al., 2018a). However, a framework that unifies the analytical expressions for ε across both turbulent and non-turbulent conditions remains absent.

Given these considerations, this study aims to investigate the effects of turbulence on inter-cloud ε–N_a relationships using LES and to explain the effects by a minimal model. We address these scientific questions: What is the role of turbulence in ε–N_a relationships? How can we quantify the role of turbulence in the ε–N_a relationships?

2 Methodology

2.1 WRF-LES model settings

This study simulates a shallow convective cloud using version 4.5.1 of the Weather Research and Forecasting (WRF) model in LES mode (Skamarock et al., 2019). Initial profiles of temperature and water vapor (Figure 1a) are derived from 16:00 LST, 2 August 2013, in the Southwestern United Kingdom (Leon et al., 2016). A random perturbation in initial potential temperature with an amplitude of 0.1 K is applied to the lowest four grid levels to stimulate turbulence (Yamaguchi and Feingold, 2012). The initial horizontal wind is set to zero to eliminate the influence of advection. Simulations in Section 3 use a grid spacing of 100 m, a time step of 0.5 s, and a domain size of 5 km × 5 km × 4.2 km. Sub-grid turbulence is treated by the turbulent kinetic energy (TKE) scheme (Deardorff, 1980). The sensitivities of our results to resolutions and sub-grid turbulence setups are examined in Text S1 of the Supporting Information (SI). Also, we adopt the Mesoscale Model 5 (MM5) similarity surface layer physics scheme (Zhang and Anthes, 1982).

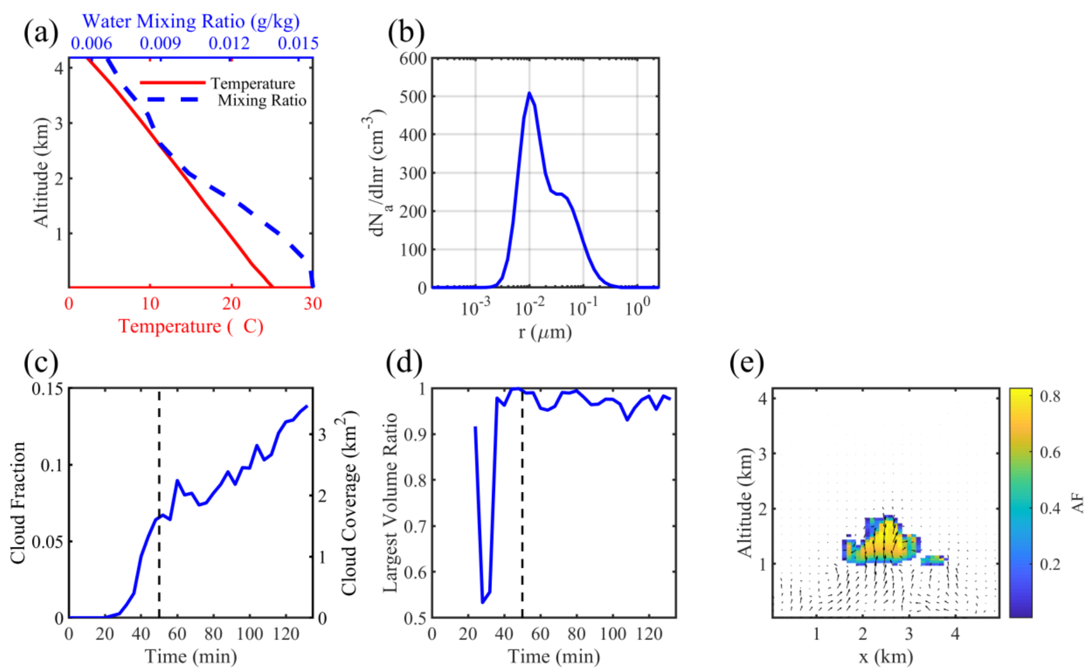

Figure 1. (a) Initial temperature and water mixing ratio profiles. (b) Initial dry aerosol particle size distribution in the simulation with aerosol number concentration (N_a) at 1,000 cm^{-3}. Time series of (c) cloud fraction, cloud coverage, and (d) the ratio of the largest cloud's volume to all clouds' volume, averaged over ten simulations. (e) A cross-section of the cloud adiabatic fraction (AF) at the 114th minute in the simulation with N_a = 1,000 cm^{-3}, taken along the central axis at y = 2.5 km.

To initiate the convective cloud, surface fluxes of potential temperature and water vapor are modified to Equations 1 and 2, respectively:

$\Phi_\theta = \Phi_{\theta,0}\, exp(-d^2/d_0^2)$, (1)

$\Phi_q = \Phi_{q,0}\, exp(-d^2/d_0^2)$, (2)

where d is the distance from the domain center, d_0 is half the domain side length, $\Phi_{\theta,0} = 0.3\ \mathrm{K\ m\ s^{-1}}$ is the maximum surface fluxes of potential temperature, and $\Phi_{q,0} = 1.2 \times 10^{-4}\ \mathrm{kg\ kg^{-1}\ s^{-1}}$ is the maximum surface fluxes of water vapor, following Chandrakar et al. (2021).

Cloud microphysics is calculated by the spectral bin microphysics (SBM) scheme (Shpund et al., 2019). We initialize N_a at the surface layer to ten values: 50, 100, 200, 500, 1,000, 2,000, 5,000, 10,000, 20,000, and 50,000 $\mathrm{cm^{-3}}$, with each value corresponding to a simulation run. Figure 1b shows the initial aerosol size distribution, adopted from the continental scenario of the SBM scheme. The SBM scheme uses Equation 3 to calculate condensational growth rate, which omits the curvature and solute effects (Khain et al., 2000):

$r\frac{dr}{dt} = \frac{1}{G}S$, (3)

where S is supersaturation, r is droplet radius, t is droplet growth time, $G = \frac{R_v T \rho_w}{e_s D_v} + \frac{L_v \rho_w}{k_d T}(\frac{L_v}{R_v T} - 1)$, ρ_w is water density, T is air temperature, D_v is vapor diffusivity, k_d is thermal conductivity, L_v is latent heat of vapor condensation, R_v is specific gas constant of water vapor, and e_s is saturation vapor pressure. To focus on the effects of turbulent condensation, we turn off collision-coalescence and sedimentation.

2.2 Cloud selection

Following previous studies (e.g., Wang et al., 2011), grids with cloud water mixing ratio greater than 0.01 $\mathrm{g\ kg^{-1}}$ are considered cloudy. We investigate the period from the 50th to the 134th minute at an interval of 4 minutes. During this period, the cloud fraction is steady relative to the preceding period (Figure 1c) and the largest individual cloud accounts for more than 90% of the total cloud volume (Figure 1d).

2.3 Adiabatic fraction calculation

Adiabatic fraction (AF) is the ratio of liquid water content (LWC) to adiabatic liquid water content ($\mathrm{LWC_{ad}}$) for each time snapshot, where $\mathrm{LWC_{ad}}$ is determined from the temperature and humidity at cloud base using Equation 8 in Pontikis (1996). An example of the spatial distribution of AF is presented in Figure 1e.

3 Results

3.1 ε–N_a relationships from LES

The left column of Figure 2 shows the vertical profiles of cloud microphysical properties, and the right column exhibits their values averaged over altitudes greater than 200 m from cloud base, where the insignificant increase in N_c with altitude (Figure 2a) indicates weak aerosol activation. Increasing N_a leads to an increase in N_c and a decrease in $\bar{r}$, which is consistent with the Twomey effect

(Figures 2a-2d). With decreasing AF of cloudy regions, both N_c and $\bar{r}$ decrease due to evaporation and dilution by mixing with ambient dry air (Figures 2b and 2d). The values of σ decrease significantly as N_a increases from 50 to 5,000 cm^{-3} (i.e., as N_c increases from 17 to 576 cm^{-3}), but have only slight variations when N_a and N_c are higher (Figures 2e and 2f), which is consistent with Lu and Seinfeld (2006). The black line in Figure 2h shows that ε decreases with increasing N_a in a low-N_a regime ($N_a < 5{,}000\mathrm{cm}^{-3}$ or $N_c < 576\mathrm{cm}^{-3}$), and increases with increasing N_a in a high-N_a regime ($N_a > 5{,}000\mathrm{cm}^{-3}$ or $N_c > 576\mathrm{cm}^{-3}$). This phenomenon does not hold for altitudes below 200 m from cloud base due to strong activation around cloud base (Figure 2g). In the more adiabatic region with higher AF, ε shows no significant variations with N_a in the low-N_a regime. This is consistent with the non-drizzling case demonstrated by Lu and Seinfeld (2006). When AF is lower, ε initially decreases and then increases with N_a (Figure 2h).

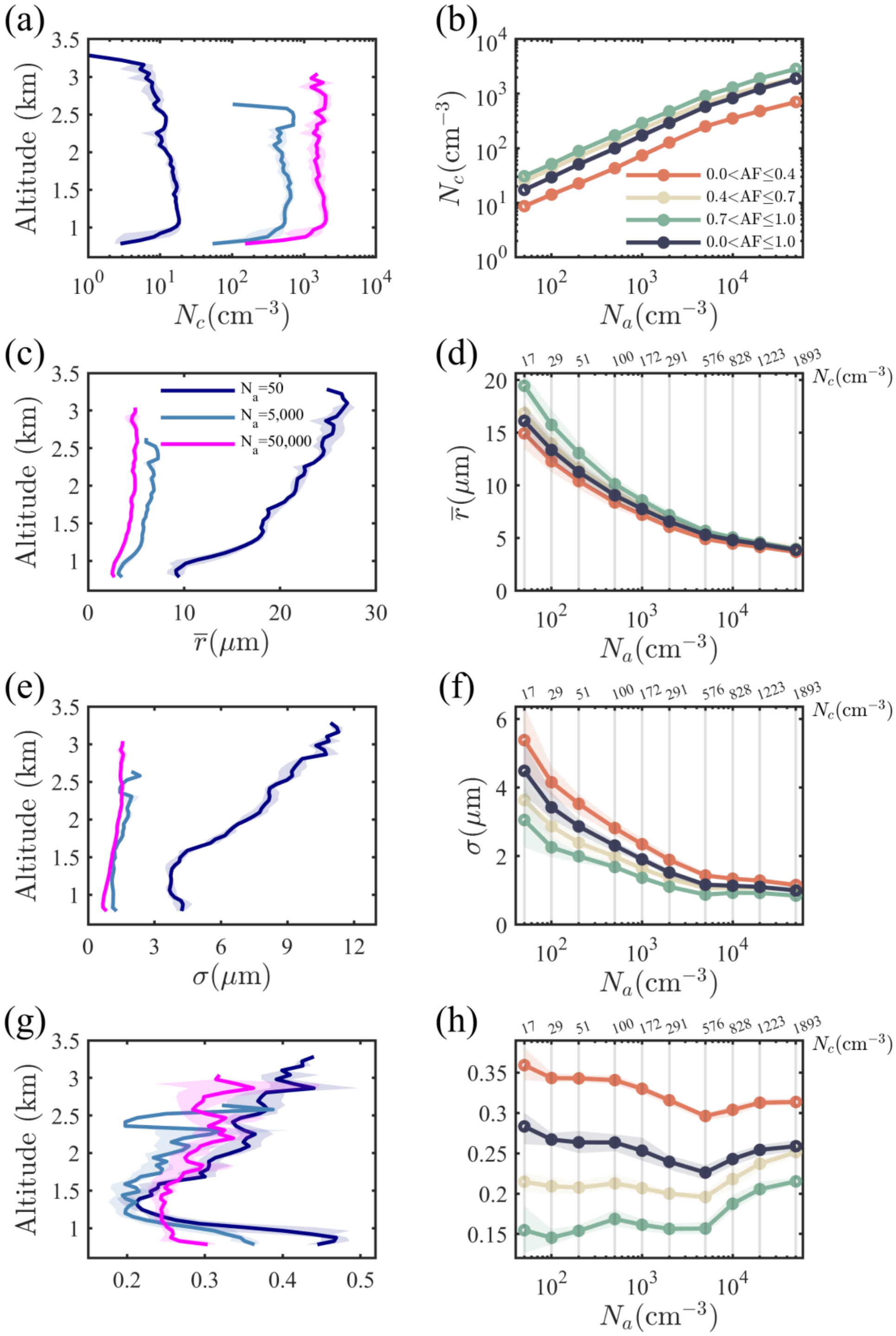

Figure 2. Vertical profiles of (a) droplet number concentration (N_c), (c) droplet mean radius ($\bar{r}$), (e) standard deviation of droplet radius (σ), and (g) droplet spectral relative dispersion (ε) under aerosol number concentration (N_a) of 50, 5,000 and 50,000 cm^{-3}. Dependence of (b) N_c, (d) $\bar{r}$, (f) σ, and (h) ε on N_a at different adiabatic fraction ranges. The top x-axes in panels d, f, and h show the corresponding cloud-mean N_c. Lines and shaded areas indicate the average and interquartile range (25% to 75%) over the studied period.

The LES reveals a negative ε–N_a correlation at low N_a in the middle and upper altitudes of the turbulent clouds, which does not exist in the middle and upper altitudes of the adiabatic clouds (Chen et al., 2018). Given that turbulence distinguishes LES from the adiabatic model, we hypothesize that turbulence causes the negative correlation at low N_a. We develop a conceptual model with a minimal set of parameters in Section 3.2 because it provides a quantitative lens through which to test this hypothesis.

3.2 An analytical expression from a minimal model

Although the LES only presents grid-scale supersaturation fluctuations, this portion still significantly influences the DSD (Lasher-Trapp et al., 2005). Using LES to examine the ε–N_a relationships therefore represents a step forward from previous studies based on adiabatic parcel theory (e.g., Chen et al., 2016, 2018; Peng et al., 2007). The minimal model presents the effects of the grid-scale supersaturation fluctuations by the varying supersaturation histories of droplets. Aerosol activation is not considered in this minimal model which aims at representing the middle and upper sections of the cloud.

We define the time-averaged supersaturation as S_m:

$$S_{\mathrm{m}} \cdot t = \int_0^t S(t')\mathrm{d}t'. \ (4)$$

By integrating Equation 3 over time after adopting Equation 4, the expression for droplet radius is:

$$[r(S_{\mathrm{m}}, r_0)]^2 = r_0^2 + 2\int_0^t S(t')\mathrm{d}t'/G = r_0^2 + 2S_{\mathrm{m}}t/G, \ (5)$$

where r_0 is the cloud droplet radius at the initial time of the minimal model. The value of S_m is positive for any existing droplet, regardless of whether $S(t')$ is exclusively positive or a mix of positive and negative values along the trajectory. To reflect droplets experiencing varying supersaturation histories, S_m is assigned a distribution rather than a single value in the minimal model. The parameter G in Equation 5 is treated as a constant, in line with prior studies (e.g., Manton, 1979; Liu et al., 2006; Celani et al., 2007; Pinsky et al., 2016; Chandrakar et al., 2018a). Text S2 in the SI further demonstrates that fluctuations in G contribute negligibly to the fluctuations in S/G compared to fluctuations in S. In subsequent derivations, an overbar denotes the average of the corresponding variable. σ and ε denote the standard deviation and the relative dispersion, respectively, with subscripts '0', 'r^2', and 'r_0^2' referring to the statistics performed on the variables r_0, r^2, and r_0^2, respectively. To minimize the set of parameters, two assumptions are made in the subsequent derivations. First, $\sigma^2 - \sigma_{r_0^2}^2$ is negligible compared to $\bar{r}^2 - \bar{r}_0^2$. Second, as used in Chandrakar et al. (2018a), ε_{r^2} and ε_{r0^2} are approximately 2ε and $2\varepsilon_0$, respectively. We will show later on that these assumptions are reasonable.

Then, averaging at both sides of Equation 5 of all the trajectories in the minimal model leads to:

$$t/G = (\overline{r^2} - \overline{r_0^2})/(2\overline{S}_{\mathrm{m}}). \ (6)$$

Therefore, the variance of r^2 is:

$$\sigma_{r^2}^2 = \sigma_{r_0^2}^2 + 4\sigma_{S_{\mathrm{m}}}^2 t^2/G^2$$

$$= \sigma_{r_0^2}^2 + (\sigma_{S_\mathrm{m}}/\bar{S}_\mathrm{m})^2(\overline{r^2} - \overline{r_0^2})^2$$

$$\approx \sigma_{r_0^2}^2 + (\sigma_{S_\mathrm{m}}/\bar{S}_\mathrm{m})^2[(\bar{r})^2 - (\overline{r_0})^2]^2. \quad (7)$$

Dividing both sides of Equation 7 by $4\bar{r}^4$, we obtain

$$\left(\frac{\varepsilon_{r^2}}{2}\right)^2 = \left(\frac{\varepsilon_{r_0^2}}{2}\right)^2\left(\frac{\overline{r_0}}{\bar{r}}\right)^4 + \left(\frac{\sigma_{S_\mathrm{m}}}{2\bar{S}_\mathrm{m}}\right)^2\left[1 - \left(\frac{\overline{r_0}}{\bar{r}}\right)^2\right]^2. \quad (8)$$

Substituting ε_{r^2} with 2ε and ε_{r0^2} with $2\varepsilon_0$ yields a simplified expression for ε:

$$\varepsilon^2 \approx \underbrace{\varepsilon_0^2\left(\frac{\overline{r_0}}{\bar{r}}\right)^4}_{E_1} + \underbrace{\left(\frac{\sigma_{S_\mathrm{m}}}{2\bar{S}_\mathrm{m}}\right)^2\left[1 - \left(\frac{\overline{r_0}}{\bar{r}}\right)^2\right]^2}_{E_2}. \quad (9)$$

Here, E_1 and E_2 represent the first and second terms on the right-hand side (RHS) of Equation 9, respectively.

The expression of E_1 does not include any information from supersaturation fluctuation and is the condensational narrowing term. E_1 is the same as the expression for ε^2 in L06 which describes the condensational narrowing effect that smaller droplets grow faster than larger ones in radius. In addition to E_1, E_2 represents the turbulence-induced supersaturation fluctuation and increases as $\bar{r}$ increases. Hence, E_2 is a turbulence-induced broadening term. While Equations 15-22 of Chandrakar et al. (2018a) also provide analytical expressions for ε under turbulent conditions, $\overline{r_0}$ and σ_0 were neglected there. Equation 9 in this study synthesizes the effects of condensational narrowing and turbulence-induced broadening. We use Equation 9 to explain the non-monotonic ε–N_a relationship in Section 3.3.

3.3 Understanding of ε–N_a relationships

Given the consistent negative $\bar{r}$–N_a relationship, we explore the ε–N_a relationship through the lens of the ε–$\bar{r}$ relationship by using the minimal model and Equation 9. To accomplish this, we determine the unknown parameters ε_0, $\overline{r_0}$ and $\sigma_{S_\mathrm{m}}/\bar{S}_\mathrm{m}$ based on the LES data.

In Equation 10, we substitute $\sigma_{S_\mathrm{m}}/\bar{S}_\mathrm{m}$ with constants c_1, c_2, and c_3 for the AF ranges of (0,0.4], (0.4,0.7], and (0.7,1.0], respectively. The values of c_1, c_2, and c_3 are constrained between 0 and 2.0, and ε_0 is constrained between 0 and 1.0, because ε is smaller than 1.0 in our LES and ε_0 and $\sigma_{S_\mathrm{m}}/(2\bar{S}_\mathrm{m})$ are the two extreme values of ε when $\bar{r}$ equals $\overline{r_0}$ and when $\bar{r}$ is positive infinity, respectively (Equation 9). We also constrain $\overline{r_0}$ between 0 and 25 μm according to Figure 2d. We solve Equation 10 to obtain the parameters:

$$\begin{cases} \text{Minimize } \sum_{i=1}^{3}\sum_{j=1}^{10}(\varepsilon_{i,j} - \varepsilon_{\mathrm{pre},i,j})^2 \\ \text{subject to} \\ \varepsilon_{\mathrm{pre},i,j}^2 = \varepsilon_0^2\left(\frac{\overline{r_0}}{\bar{r}_{i,j}}\right)^4 + \frac{c_i^2}{4}\left[1 - \left(\frac{\overline{r_0}}{\bar{r}_{i,j}}\right)^2\right]^2,\ i = 1,2,3 \\ 0 \le c_i < 2.0, i = 1,2,3 \\ 0 \le \varepsilon_0 < 1.0 \\ 0 \le \overline{r_0} < 25.0\ \mu\mathrm{m} \end{cases}, \quad (10)$$

where $i = 1,2,3$ correspond to the AF ranges of (0,0.4], (0.4,0.7], and (0.7,1.0], respectively, and $j = 1,2,\ldots,10$ correspond to the simulations with N_a values of 50, 100, ..., and 50,000 cm^{-3}, respectively. $\varepsilon_{i,j}$ and $\bar{r}_{i,j}$ represent the droplet spectral relative dispersion and mean radius averaged over the altitudes greater than 200 m from cloud base in LES, respectively, and $\varepsilon_{\mathrm{pre},i,j}$ represents the predictions by curve fitting. The optimal parameters obtained are c_1=0.717, c_2=0.438, c_3=0.324, ε_0=0.589, and $\bar{r}_0$=2.25 μm. The predicted ε in the left panel of Figure 3 shows good agreement with that from LES, with a coefficient of determination (R^2) of 0.97 and a root mean square error (RMSE) of 0.02, across all 660 data points used in the fitting (comprising 10 N_a values, 3 AF ranges, and 22 time snapshots). Also, with the increase in AF, c_i decreases, which describes the less supersaturation fluctuations in the more adiabatic region, consistent with Chen et al. (2021).

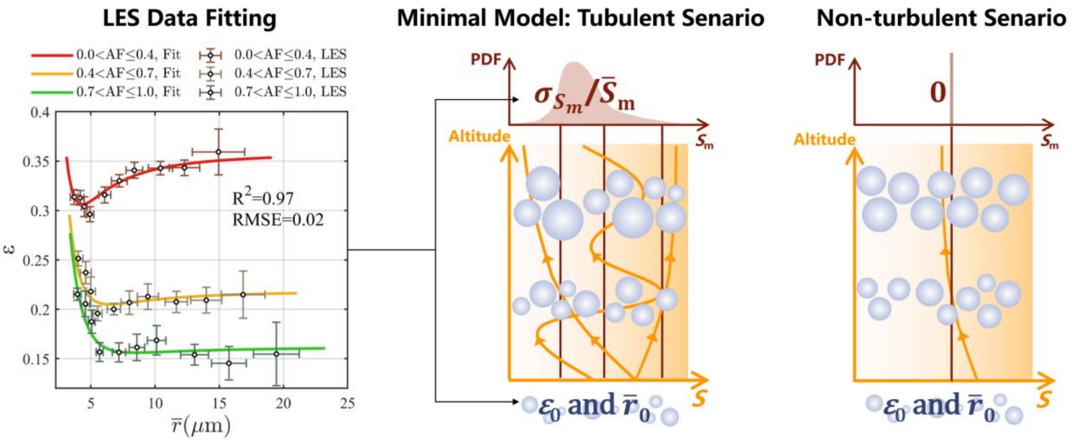

Figure 3. In the left panel, each marker with error bars represents the average and standard deviation of ε and $\bar{r}$ based on LES data. The ten markers from left to right at the same AF range correspond to ten simulations with aerosol concentrations from high to low. Solid lines represent the fitting results. The fitted parameters initialize the minimal model (the middle panel). Yellow lines illustrate droplets' historical supersaturation, with its time-mean value, S_m, represented by dark red lines. The right panel depicts the droplet growth under a non-turbulent assumption.

Figure 4 presents the results from Equation 9 with ε_0 and $\bar{r}_0$ derived from the LES data, in which the white dotted lines represent c_i derived from the LES data. The white solid lines indicate the minimum values of ε at each $\sigma_{S_m}/\bar{S}_m$. In Figure 4a, ε first decreases and then increases with increasing N_a (i.e., decreasing $\bar{r}$) at given $\sigma_{S_m}/\bar{S}_m$. This is consistent with Figure S3 using the original definition of ε, which verifies the non-monotonic relationship does not depend on assumptions made in the derivations of Equation 9 (see Text S3 in the SI for details).

Figures 4b and 4c elucidate aerosols' modulations on ε. The increase in E_1 with increasing N_a (i.e., decreasing $\bar{r}$) in Figure 4b demonstrates the effect of increasing aerosols on suppressing the intensity of condensational narrowing. The decrease in E_2 with increasing N_a (i.e., decreasing $\bar{r}$) in Figure 4c indicates the effect of increasing aerosols on suppressing the intensity of turbulence-induced broadening. In the low-N_a regime (to the right of the white solid line), the suppression of turbulence-induced broadening is stronger than that of condensational narrowing, causing ε to decrease with rising N_a. Conversely, in the high-N_a regime (to the left of the white solid line), the suppression of condensational narrowing becomes more pronounced than that of turbulence-induced broadening, resulting in ε increasing as N_a increases. The regimes are determined by comparing

$\overline{r_0}/\bar{r}$ to a threshold $(\overline{r_0}/\bar{r})_{\text{trans}}$, which is obtained by taking the derivative of Equation 9 with respect to $\bar{r}$:

$$(\overline{r_0}/\bar{r})_{\text{trans}} = \frac{\sigma_{s_\text{m}}/\bar{S}_\text{m}}{\sqrt{4\varepsilon_0^2+(\sigma_{s_\text{m}}/\bar{S}_\text{m})^2}}. \quad (11)$$

Droplets with $\overline{r_0}/\bar{r} < (\overline{r_0}/\bar{r})_{\text{trans}}$ belong to the low-N_a regime, while those with $\overline{r_0}/\bar{r} > (\overline{r_0}/\bar{r})_{\text{trans}}$ belong to the high-N_a regime.

In the nearly adiabatic cloud zone (the lowest dotted line in Figure 4), the decrease in E_2 with increasing N_a is weak due to the small value of $\sigma_{s_\text{m}}/\bar{S}_\text{m}$, so the scenario approaches that depicted by the adiabatic theory that ε monotonically increases with increasing N_a. This is consistent with the green line in Figure 2h.

Figure 4d shows a sub-regime within the high-N_a regime, in which as $\bar{r}$ decreases, σ decreases in a smaller amplitude than $\bar{r}$, resulting in ε increasing with rising N_a (i.e., decreasing $\bar{r}$). This sub-regime aligns with the cases with $N_\text{a} > 5{,}000\text{cm}^{-3}$ in Figure 2f.

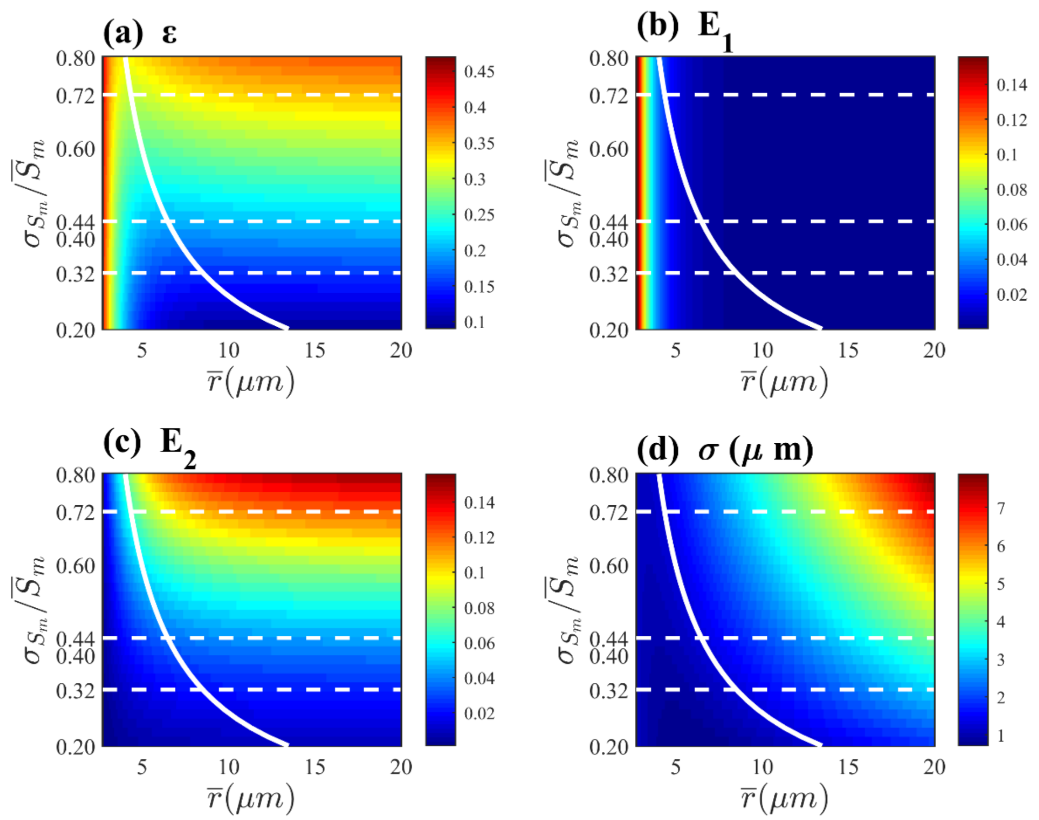

Figure 4. Joint dependence on droplet mean radius ($\bar{r}$) and relative dispersion of droplet's time-averaged supersaturation ($\sigma_{s_\text{m}}/\bar{S}_\text{m}$) of (a) droplet spectral relative dispersion (ε), (b) condensational narrowing term (E_1), (c) turbulence-induced broadening term (E_2), and (d) the standard deviation of droplet radius (σ, obtained by $\varepsilon \cdot \bar{r}$) based on Equation 9. The white dotted lines from up to down correspond to $\sigma_{s_\text{m}}/\bar{S}_\text{m}$ at adiabatic ranges of (0,0.4], (0.4,0.7], and (0.7,1.0], respectively. The white solid line indicates the minimum point of ε.

Regime-dependent cloud properties were also reported in prior studies. Both approaches from Reutter et al. (2009) and Prabhakaran et al. (2020) highlight that N_a impacts the magnitude of supersaturation. In regimes with low N_a values, the magnitude of supersaturation is large, resulting in a high activation fraction (Reutter et al., 2009; Prabhakaran et al., 2020; Shawon et al., 2021) and an increase in ε with increasing N_a at cloud base (Chen et al., 2016, 2018). As N_a rises, the magnitude of supersaturation diminishes, leading to the formation of other regimes. Rather, this study emphasizes that lower N_a enhances the influence of turbulence on cloud droplet size distribution. As N_a decreases (i.e., $\bar{r}$ in Equation 9 increases), ε deviates from the non-turbulent ε in L06 and ultimately shows the opposite trend to the non-turbulent ε in L06—specifically, an increase with decreasing N_a in the low-N_a regime.

4 Concluding remarks

This study investigates the non-monotonic relationship between ε and N_a at the middle and higher altitudes in turbulent clouds using idealized LES simulations. The effects of collision-coalescence and sedimentation are not considered. Our results demonstrate a clear regime dependence: in the low-N_a regime ($N_\mathrm{a} < 5{,}000\mathrm{cm}^{-3}$ or $N_\mathrm{c} < 576\mathrm{cm}^{-3}$), ε decreases with increasing N_a, while in the high-N_a regime ($N_\mathrm{a} > 5{,}000\mathrm{cm}^{-3}$ or $N_\mathrm{c} > 576\mathrm{cm}^{-3}$), ε exhibits an increasing trend with N_a. The high-N_a regime behavior aligns with the findings of L06, whereas the low-N_a regime reveals a trend opposite to L06.

To theoretically present and explain this relationship, we derive an analytical expression for ε by combining both condensational narrowing and turbulence broadening together. The expression demonstrates that in the low-N_a regime, ε decreases with increasing N_a because the increase in N_a weakens the intensity of turbulence-induced broadening to a greater extent than it weakens condensational narrowing. However, in the high-N_a regime, ε increases with increasing N_a, because the increase in N_a weakens the intensity of condensational narrowing more significantly than it weakens turbulence-induced broadening.

Using in-situ observations, Figure 16 in Lu and Seinfeld (2006) showed a similar phenomenon that ε decreases with increasing N_c for the marine stratocumulus with $5\mathrm{cm}^{-3} \le N_\mathrm{c} \le 296\mathrm{cm}^{-3}$, and slightly increases with increasing N_c for the continental stratocumulus with $12\mathrm{cm}^{-3} \le N_\mathrm{c} \le 693\mathrm{cm}^{-3}$.

Nevertheless, directly validating our conclusions with observations remains challenging due to two key limitations. From a theoretical perspective, our LES-derived framework focuses on condensational growth in large-eddy turbulent environments. However, real-world processes such as collision-coalescence complicate the comparison of our theory with observations. From an observational standpoint, in-situ measurements of ε–N_a relationships struggle to isolate aerosol-induced droplet changes due to the confounding effects of meteorological variability.

The experimental approach helps bridge these gaps. The Pi chamber produces supersaturation fluctuations within a range that is reasonable for atmospheric conditions, making it to some extent representative of real clouds (Chandrakar et al., 2016; Prabhakaran et al., 2022). Chandrakar et al. (2018b) conducted a controlled experiment using a cloud chamber with different aerosol injection rates with minimal impacts from collision-coalescence, as reflected by the volume mean radius being smaller than 12 μm. They demonstrated that an increase in N_c leads to an increase in k (i.e., a decrease in ε) when N_c is below ~600 cm^{-3}, and a decrease in k (i.e., an increase in ε) when N_c is higher than ~600 cm^{-3}, which supports our conclusion. In future studies, we will incorporate the effects of collision-coalescence and sedimentation in our modeling approach and validate the results using meteorologically constrained observations.

The proposed theoretical framework reconciles the widths of DSD in both non-turbulent and turbulent scenarios and offers a potential way for parameterizing the width of DSD in large-scale earth system models (e.g., GCM) to better study aerosol-cloud interactions. A benefit of using LES in this study is its ability to present the vertical variations of properties from cloud base to cloud top and from cloud core to cloud edge alongside their sensitivity to N_a. In the future study, we plan to use direct numerical simulation (DNS), which resolves the full spectrum of turbulence, to provide higher-fidelity results within specific portions of the cloud (e.g., Götzfried et al., 2017; Thomas et al., 2024). While the microphysics is currently handled by the SBM scheme, the super-droplet method (SDM), which enables backward tracking of droplets, will be used in our future work to investigate the magnitude of $\sigma_{S_m}/\bar{S}_m$ and the impact of collision-coalescence on ε following the SDM track (Yin et al., 2024). The implications of the newly identified ε–N_a relationship—particularly the predominant negative correlation observed in the more frequently occurring low-N_a regime—for global cloud shortwave radiative feedbacks also need investigations.

Acknowledgments

This research is supported by the National Natural Science Foundation of China (42325503, 42405076), and the Startup Foundation for Introducing Talent of NUIST (2024r099). The appointment of Chunsong Lu at Nanjing University of Information Science & Technology is partially supported by the Jiangsu Specially-Appointed Professor (R2024T01). We acknowledge the High Performance Computing Center of Nanjing University of Information Science & Technology for their support of this work.

References

Andrejczuk, M., Grabowski, W. W., Malinowski, S. P., & Smolarkiewicz, P. K. (2004). Numerical Simulation of Cloud–Clear Air Interfacial Mixing. *Journal of the Atmospheric Sciences*, 61(14), 1726-1739. https://doi.org/10.1175/1520-0469(2004)061<1726:NSOCAI>2.0.CO;2

Celani, A., Mazzino, A., Seminara, A., & Tizzi, M. (2007). Droplet condensation in two-dimensional Bolgiano turbulence. *Journal of Turbulence*, 8(17), 1-9. https://doi.org/10.1080/14685240601105716

Chandrakar, K. K., Cantrell, W., Chang, K., Ciochetto, D., Niedermeier, D., Ovchinnikov, M., Shaw, R. A., & Yang, F. (2016). Aerosol indirect effect from turbulence-induced broadening of cloud-droplet size distributions. *Proceedings of the National Academy of Sciences*, 113(50), 14243-14248. https://doi.org/10.1073/pnas.1612686113

Chandrakar, K. K., Cantrell, W., & Shaw, R. A. (2018a). Influence of Turbulent Fluctuations on Cloud Droplet Size Dispersion and Aerosol Indirect Effects. *Journal of Atmospheric Sciences*, 75(9), 3191-3209. https://doi.org/10.1175/JAS-D-18-0006.1

Chandrakar, K. K., Cantrell, W., Kostinski, A. B., & Shaw, R. A. (2018b). Dispersion Aerosol Indirect Effect in Turbulent Clouds: Laboratory Measurements of Effective Radius. *Geophysical Research Letters*, 45(19), 10738-10745. https://doi.org/10.1029/2018GL079194

Chandrakar, K. K., Grabowski, W. W., Morrison, H., & Bryan, G. H. (2021). Impact of Entrainment Mixing and Turbulent Fluctuations on Droplet Size Distributions in a Cumulus Cloud: An Investigation Using Lagrangian Microphysics with a Subgrid-Scale Model. *Journal of the Atmospheric Sciences*, 78(9), 2983-3005. https://doi.org/10.1175/JAS-D-20-0281.1

Chen, J., Y. Liu, M. Zhang, and Y. Peng (2016), New understanding and quantification of the regime dependence of aerosol-cloud interaction for studying aerosol indirect effects, *Geophysical Research Letters*, 43(4), 1780–1787. https://doi.org/10.1002/2016gl067683

Chen, J., Liu, Y., Zhang, M., & Peng, Y. (2018). Height dependency of aerosol-cloud interaction regimes. *Journal of Geophysical Research: Atmospheres*, 123, 491–506. https://doi.org/10.1002/2017jd027431

Chen, S., Xue, L., & Yau, M. K. (2021). Hygroscopic Seeding Effects of Giant Aerosol Particles Simulated by the Lagrangian-Particle-Based Direct Numerical Simulation. *Geophysical Research Letters*, 48(20), e2021GL094621. https://doi.org/10.1029/2021GL094621

Chen, Y., (2025). DATA FOR Turbulence-induced Non-Monotonic Influence of Aerosols on Cloud Droplet Size Distribution (v1.22). *Zenodo*. https://doi.org/10.5281/zenodo.15245733

Deardorff, J. W. (1980). Stratocumulus-Capped Mixed Layers Derived from a 3-Dimensional Model. *Boundary-Layer Meteorology*, 18(4), 495-527. https://doi.org/10.1007/bf00119502

Grabowski, W. W., & Wang, L. P. (2013). Growth of Cloud Droplets in a Turbulent Environment. *Annual Review of Fluid Mechanics*, 45, 293-324. https://doi.org/10.1146/annurev-fluid-011212-140750

Götzfried, P., Kumar, B., Shaw, R. A., & Schumacher, J. (2017). Droplet dynamics and fine-scale structure in a shearless turbulent mixing layer with phase changes. *Journal of Fluid Mechanics*, 814, 452-483. https://doi.org/10.1017/jfm.2017.23

Hu, A. Z., Igel, A. L., Chuang, P. Y., & Witte, M. K. (2021). Recognition of Inter-Cloud Versus Intra-Cloud Controls on Droplet Dispersion With Applications to Microphysics Parameterization. *Journal of Geophysical Research: Atmospheres*, 126(18), e2021JD035180. https://doi.org/10.1029/2021JD035180

Igel, A. L., & van den Heever, S. C. (2017). The Importance of the Shape of Cloud Droplet Size Distributions in Shallow Cumulus Clouds. Part I: Bin Microphysics Simulations. *Journal of the Atmospheric Sciences*, 74(1), 249-258. https://doi.org/10.1175/JAS-D-15-0382.1

Jensen, J. B., & Baker, M. B. (1989). A Simple Model of Droplet Spectral Evolution during Turbulent Mixing. *Journal of Atmospheric Sciences*, 46(18), 2812-2829. https://doi.org/10.1175/1520-0469(1989)046<2812:ASMODS>2.0.CO;2

Jeffery, C. A., Reisner, J. M., & Andrejczuk, M. (2007). Another look at stochastic condensation for subgrid cloud modeling: Adiabatic evolution and effects. *Journal of the Atmospheric Sciences*, 64(11), 3949-3969. https://doi.org/10.1175/2006JAS2147.1

Khain, A., Ovtchinnikov, M., Pinsky, M., Pokrovsky, A., & Krugliak, H. (2000). Notes on the state-of-the-art numerical modeling of cloud microphysics. *Atmospheric Research,* 55(3-4), 159-224. https://doi.org/10.1016/s0169-8095(00)00064-8

Kumar, B., Janetzko, F., Schumacher, J., & Shaw, R. A. (2012). Extreme responses of a coupled scalar-particle system during turbulent mixing. *New Journal of Physics*, 14, Article 115020. https://doi.org/10.1088/1367-2630/14/11/115020

Kumar, B., Götzfried, P., Suresh, N., Schumacher, J., & Shaw, R. A. (2018). Scale Dependence of Cloud Microphysical Response to Turbulent Entrainment and Mixing. *Journal of Advances in Modeling Earth Systems*, 10(11), 2777-2785. https://doi.org/10.1029/2018MS001487

Kumar, B., Ranjan, R., Yau, M. K., Bera, S., & Rao, S. A. (2021). Impact of high- and low-vorticity turbulence on cloud-environment mixing and cloud microphysics processes. *Atmospheric Chemistry and Physics*, 21(16), 12317-12329. https://doi.org/10.5194/acp-21-12317-2021

Lasher-Trapp, S. G., Cooper, W. A., & Blyth, A. M. (2005). Broadening of droplet size distributions from entrainment and mixing in a cumulus cloud. *Quarterly Journal of the Royal Meteorological Society*, 131(605), 195-220. https://doi.org/10.1256/qj.03.199

Leon, D. C., French, J. R., Lasher-Trapp, S., Blyth, A. M., Abel, S. J., Ballard, S., Barrett, A., Bennett, L. J., Bower, K., Brooks, B., Brown, P., Charlton-Perez, C., Choularton, T., Clark, P., Collier, C., Crosier, J., Cui, Z. Q., Dey, S., Dufton, D., . . . Young, G. (2016). The Convective Precipitation Experiment (COPE): Investigating the Origins of Heavy Precipitation in the Southwestern United Kingdom. *Bulletin of the American Meteorological Society*, 97(6), 1003-1020. https://doi.org/10.1175/bams-d-14-00157.1

Liu, Y., and Daum, P. H. (2002). Anthropogenic aerosols: Indirect warming effect from dispersion forcing. *Nature*, 419(6907), 580–581. https://doi.org/10.1038/419580a

Liu, Y., Daum, P. H., Yum, S. S. (2006). Analytical expression for the relative dispersion of the cloud droplet size distribution. *Geophysical Research Letters*, 33(2), L02810. https://doi.org/10.1029/2005gl024052

Liu, Y., Daum, P. H., & Lu, C. (2014). Comment on “Cloud droplet spectral width relationship to CCN spectra and vertical velocity” by Hudson et al. *Journal of Geophysical Research: Atmospheres*, 119(4), 1874-1877. https://doi.org/10.1002/2012JD019207

Lu, M.-L., & Seinfeld, J. H. (2006). Effect of aerosol number concentration on cloud droplet dispersion: A large-eddy simulation study and implications for aerosol indirect forcing. *Journal of Geophysical Research*, 111(D2). https://doi.org/10.1029/2005jd006419

Manton, M. J. (1979). On the broadening of a droplet distribution by turbulence near cloud base. *Quarterly Journal of the Royal Meteorological Society*, 105(446), 899-914. https://doi.org/10.1002/qj.49710544613

Peng, Y., & Lohmann, U. (2003). Sensitivity study of the spectral dispersion of the cloud droplet size distribution on the indirect aerosol effect. *Geophysical Research Letters*, 30(10). https://doi.org/10.1029/2003GL017192

Peng, Y. R., Lohmann, U., Leaitch, R., & Kulmala, M. (2007). An investigation into the aerosol dispersion effect through the activation process in marine stratus clouds. *Journal of Geophysical Research-Atmospheres*, 112(D11), Article D11117. https://doi.org/10.1029/2006jd007401

Pinsky, M., Khain, A., & Korolev, A. (2016). Theoretical analysis of mixing in liquid clouds - Part 3: Inhomogeneous mixing. *Atmospheric Chemistry and Physics*, 16(14), 9273-9297. https://doi.org/10.5194/acp-16-9273-2016

Pontikis, C., & Hicks, E. (1992). Contribution to the cloud droplet effective radius parameterization. *Geophysical Research Letters*, 19(22), 2227-2230. https://doi.org/10.1029/92GL02283

Pontikis, C. A. (1996). Parameterization of the droplet effective radius of warm layer clouds. *Geophysical Research Letters*, 23(19), 2629–2632. https://doi.org/10.1029/96GL02452

Prabhakaran, P., Shawon, A. S. M., Kinney, G., Thomas, S., Cantrell, W., & Shaw, R. A. (2020). The role of turbulent fluctuations in aerosol activation and cloud formation. *Proceedings of the National Academy of Sciences*, 117(29), 16831-16838. https://doi.org/10.1073/pnas.2006426117

Prabhakaran, P., Thomas, S., Cantrell, W., Shaw, R. A., & Yang, F. (2022). Sources of Stochasticity in the Growth of Cloud Droplets: Supersaturation Fluctuations versus Turbulent Transport. *Journal of the Atmospheric Sciences*, 79(12), 3145-3162. https://doi.org/10.1175/JAS-D-22-0051.1

Rotstayn, L. D., & Liu, Y. (2003). Sensitivity of the First Indirect Aerosol Effect to an Increase of Cloud Droplet Spectral Dispersion with Droplet Number Concentration. *Journal of Climate*, 16(21), 3476-3481. https://doi.org/10.1175/1520-0442(2003)016<3476:SOTFIA>2.0.CO;2

Rotstayn, L. D., & Liu, Y. (2005). A smaller global estimate of the second indirect aerosol effect. *Geophysical Research Letters*, 32(5). https://doi.org/10.1029/2004GL021922

Shawon, A. S. M., Prabhakaran, P., Kinney, G., Shaw, R. A., & Cantrell, W. (2021). Dependence of Aerosol-Droplet Partitioning on Turbulence in a Laboratory Cloud. *Journal of Geophysical Research: Atmospheres*, 126(5), e2020JD033799. https://doi.org/10.1029/2020JD033799

Seinfeld, J. H., Bretherton, C., Carslaw, K. S., Coe, H., DeMott, P. J., Dunlea, E. J., Feingold, G., Ghan, S., Guenther, A. B., Kahn, R., Kraucunas, I., Kreidenweis, S. M., Molina, M. J., Nenes, A., Penner, J. E., Prather, K. A., Ramanathan, V., Ramaswamy, V., Rasch, P. J., ... Wood, R. (2016). Improving our fundamental understanding of the role of aerosol-cloud interactions in the climate system. *Proceedings of the National Academy of Sciences of the United States of America*, 113(21), 5781-5790. https://doi.org/10.1073/pnas.1514043113

Shpund, J., Khain, A., Lynn, B., Fan, J. W., Han, B., Ryzhkov, A., Snyder, J., Dudhia, J., & Gill, D. (2019). Simulating a Mesoscale Convective System Using WRF With a New Spectral Bin Microphysics: 1: Hail vs Graupel. *Journal of Geophysical Research: Atmospheres*, 124(24), 14072-14101. https://doi.org/10.1029/2019jd030576

Skamarock, C., Klemp, B., Dudhia, J., Gill, O., Liu, Z., Berner, J., Wang, W., Powers, G., Duda, G., Barker, D. M., & Huang, X. (2019). *A Description of the Advanced Research WRF Model Version 4*. National Center for Atmospheric Research. https://doi.org/10.5065/1dfh-6p97

Smagorinsky, J. (1963). General Circulation Experiments with the Primitive Equations: I. The Basic Experiment. *Monthly Weather Review*, 91(3), 99-164. https://doi.org/10.1175/1520-0493(1963)091<0099:GCEWTP>2.3.CO;2

Thomas, S., Ovchinnikov, M., Yang, F., van der Voort, D., Cantrell, W., Krueger, S. K., & Shaw, R. A. (2019). Scaling of an Atmospheric Model to Simulate Turbulence and Cloud Microphysics in the Pi Chamber. *Journal of Advances in Modeling Earth Systems*, 11(7), 1981-1994. https://doi.org/10.1029/2019MS001670

Thomas, L., Kumar, B., Zuend, A., Hassan-Barthaux, D., & Rao, S. A. (2024). CCN activation in homogeneous isotropic turbulence: Response to particle characteristics and environmental conditions. *Atmospheric Research*, 297, 107095. https://doi.org/10.1016/j.atmosres.2023.107095

Wang, M., Peng, Y., Liu, Y., Liu, Y., Xie, X., & Guo, Z. (2020). Understanding cloud droplet spectral dispersion effect using empirical and semi-analytical parameterizations in NCAR CAM5. 3. *Earth and Space Science*, 7(8), e2020EA001276. https://doi.org/10.1029/2020EA001276

Wang, X., Xue, H., Fang, W, Zheng, G. (2011). A study of shallow cumulus cloud droplet dispersion by large eddy simulations. *Journal of Meteorological Research*, 25(2), 166–175. https://doi.org/10.1007/s13351-011-0024-9

Xie, X., & Liu, X. (2011). Effects of spectral dispersion on clouds and precipitation in mesoscale convective systems. *Journal of Geophysical Research: Atmospheres*, 116(D6). https://doi.org/10.1029/2010JD014598

Yamaguchi, T., & Feingold, G. (2012). Technical note: Large-eddy simulation of cloudy boundary layer with the Advanced Research WRF model. *Journal of Advances in Modeling Earth Systems*, 4(3). https://doi.org/10.1029/2012MS000164

Yin, C., Shima, S.-i., Xue, L., & Lu, C. (2024). Simulation of marine stratocumulus using the super-droplet method: numerical convergence and comparison to a double-moment bulk scheme using SCALE-SDM 5.2. 6-2.3. 1. *Geoscientific Model Development*, 17(13), 5167-5189. https://doi.org/10.5194/gmd-17-5167-2024

Yin, J., Wang, D., Zhai, G., Wang, H., Xu, H., & Liu, C. (2022). A modified double-moment bulk microphysics scheme geared toward the East Asian Monsoon region. *Advances in Atmospheric Sciences*, 39(9), 1451-1471. https://doi.org/10.1007/s00376-022-1402-1

Zhang, D.; Anthes, R. A. (1982). A high-resolution model of the planetary boundary layer—sensitivity tests and comparisons with SESAME-79 data. *Journal of Applied Meteorology*, 21(11), 1594–1609. https://doi.org/10.1175/1520-0450(1982)021<1594:AHRMOT>2.0.CO;2

Supporting Information

Text S1: Details of the large eddy simulations

The activation process in the SBM scheme is implemented as follows: Particles within an aerosol bin are transferred to a cloud droplet bin if their radius r_N exceeds the critical activation radius. Upon activation, these particles are given a preset cloud droplet radius. The SBM scheme operates in a 1-D configuration, as it does not compute or track solute quantities within individual cloud droplet bins. (Khain et al., 2000)

The simulations in Section 3 have shown a non-monotonic relationship between ε and N_a. To test its sensitivity to resolutions and sub-grid turbulence setups, we conduct two additional sets of simulations. Their settings are shown in Table S1. In the TKE_DX50 experiments, the grid spacing is reduced to 50 m, with a temporal resolution of 0.3 s to maintain numerical stability. In the SMA_DX100 experiments, sub-grid turbulence is treated by the 3D Smagorinsky scheme (Smagorinsky, 1963) instead of the TKE scheme. The black lines in Figures S1f and S2f show that, averaged over altitudes above 200 m from cloud base, ε first decreases and then increases with increasing N_a, which shows the robustness our simulated results.

Table S1. The settings for sensitivity experiments.

	Sub-grid turbulence scheme	Horizontal resolution	Vertical resolution	Time step
TKE_DX100	TKE	100 m × 100 m.	The domain is 4.2 km thick with 80 layers.	0.5 s
TKE_DX50	TKE	50 m × 50 m.	The domain is 4.2 km thick with 180 layers.	0.3 s
SMA_DX100	3D Smagorinsky	100 m × 100 m.	The domain is 4.2 km thick with 80 layers.	0.5 s

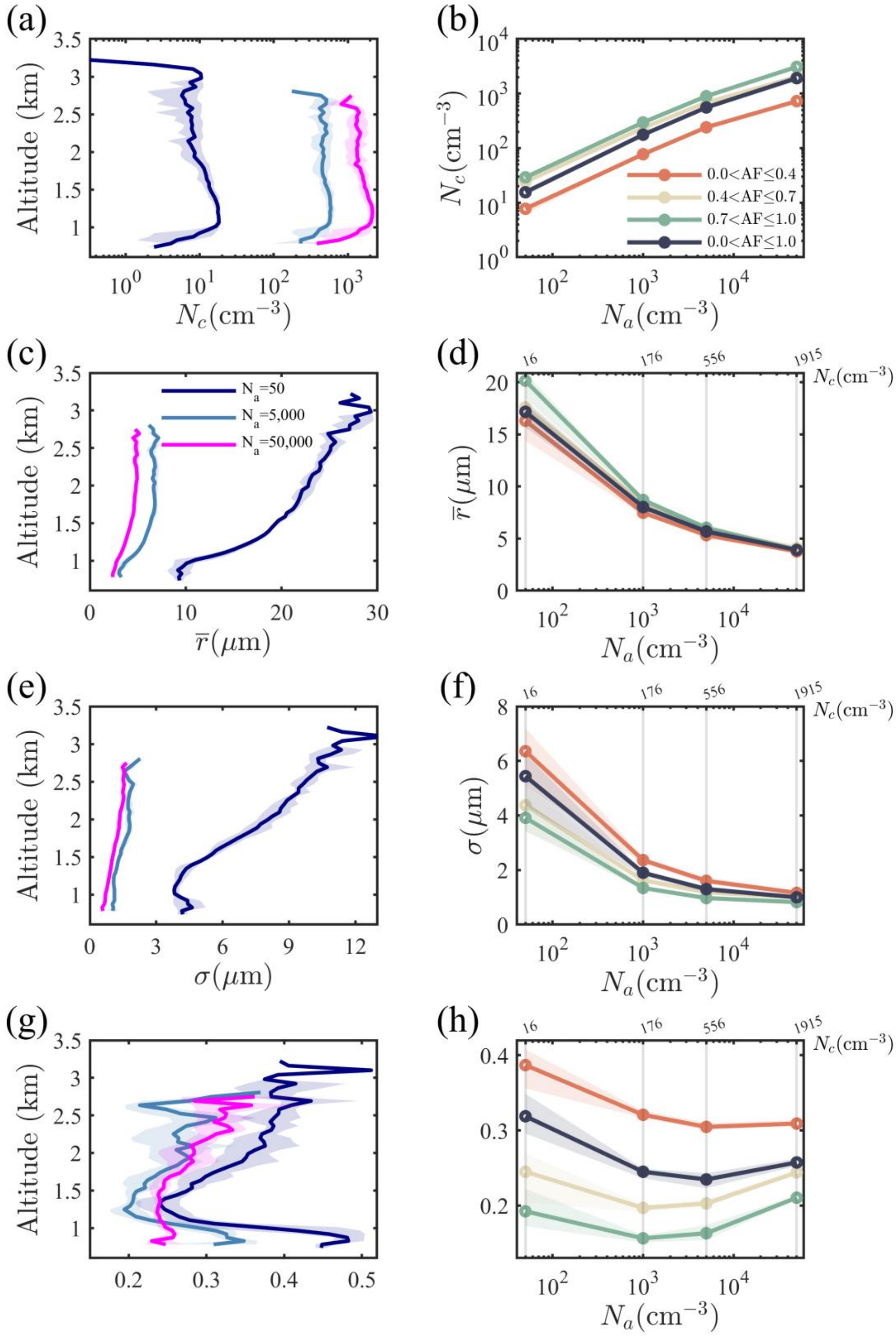

Figure S1. Droplet number concentration (N_c), droplet mean radius ($\bar{r}$), standard deviation of droplet radius (σ), and droplet spectral relative dispersion from SMA_DX100 experiments. Vertical profiles of (a) N_c, (c) $\bar{r}$, (e) σ, and (g) ε under aerosol number concentration (N_a) of 50, 5,000 and 50,000 cm^{-3}. Dependence of (b) N_c, (d) $\bar{r}$, (f) σ, and (h) ε on N_a at different adiabatic fraction ranges. Lines and shaded areas indicate the average and interquartile range (25% to 75%) over the studied period.

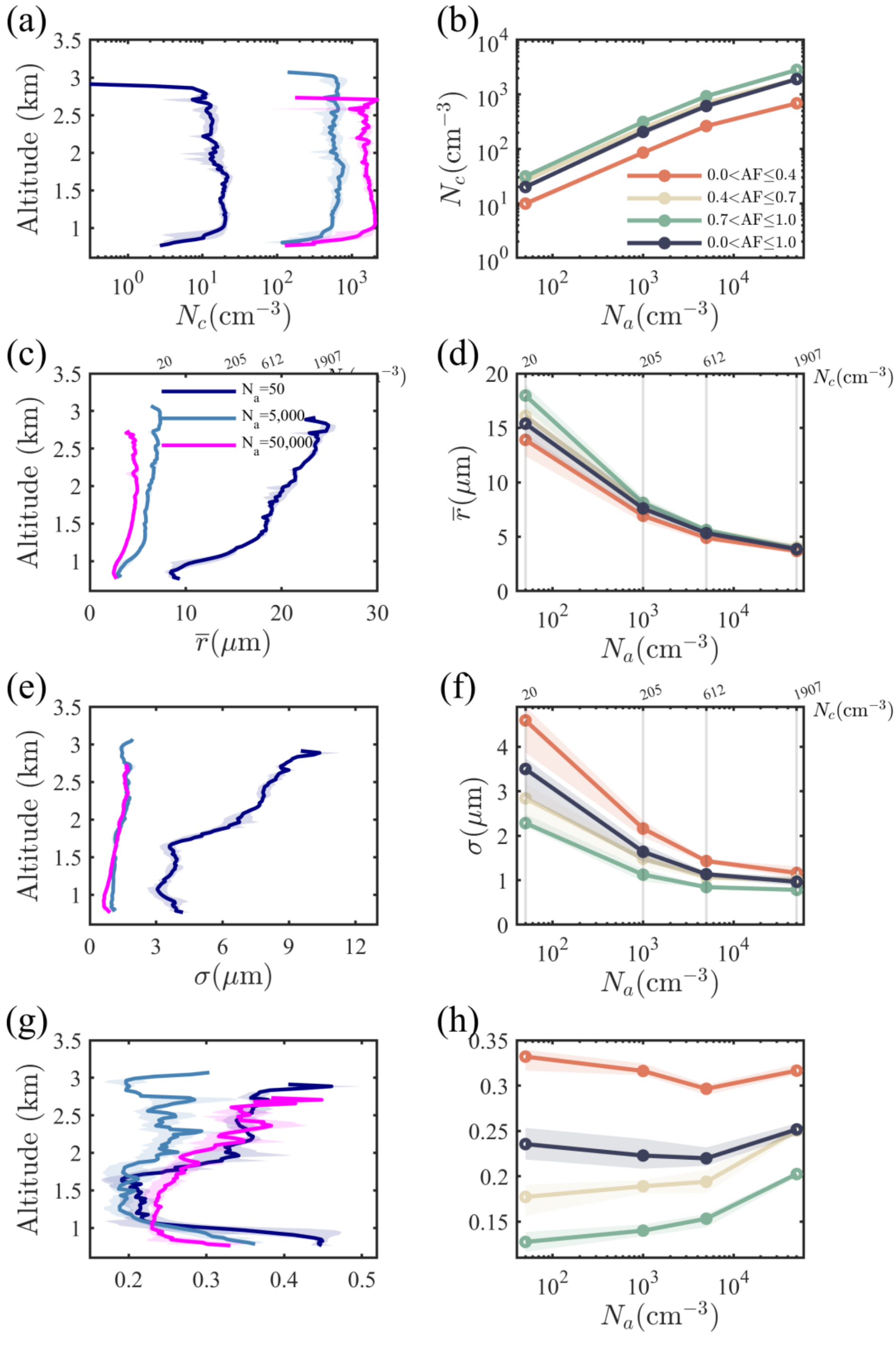

Figure S2. Droplet number concentration (N_c), droplet mean radius ($\bar{r}$), standard deviation of droplet radius (σ), and droplet spectral relative dispersion from TKE_DX50 experiments. Vertical profiles of (a) N_c, (c) $\bar{r}$, (e) σ, and (g) ε under aerosol number concentration (N_a) of 50, 5,000 and 50,000 cm^{-3}. Dependence of (b) N_c, (d) $\bar{r}$, (f) σ, and (h) ε on N_a at different adiabatic fraction ranges. Lines and shaded areas indicate the average and interquartile range (25% to 75%) over the studied period.

Text S2: Relative importance of G

Table S2 justifies our approximation of G to a constant during derivations. Over our studied period, the standard deviation of S/G within the cloud is 1.5269×10^{-6}% cm^2 s^{-1} on average. When each grid's G value is substituted by cloud-average G, the standard deviation of S/G is slightly increased to 1.5687×10^{-6}% cm^2 s^{-1}. While it is decreased to 9.1189×10^{-9}% cm^2 s^{-1} when substituting each grid's S with cloud-average S. So, the fluctuations in G are insignificant for the fluctuations in S/G. The 2nd row in Table S2 indicates that when we change the cloud selection criterion, the fluctuations in G still do not contribute significantly to the fluctuations in S/G.

Table S2. The 2nd column shows the standard deviation of the ratio of supersaturation (S) to the growth coefficient (G). Each value of S/G is taken from one grid in WRF outputs. The 2nd row uses the grids with cloud water mixing ratio (Q_c) greater than 0.01 g kg^{-1}, and the 3rd row uses the grids with $S > 0$. The 3rd column is the same as the 2nd column but uses the average G to substitute each grid's G value. The 4th column is the same as the 2nd column but uses the average S to substitute each grid's S value. The units of S is %, and the units of G is cm^{-2}s.

Grid Selection Criterion	STD(S/G)	STD(S/AVE(G))	STD(AVE(S)/G)
$Q_c > 0.01$ g kg^{-1}	1.5269×10^{-6}	1.5687×10^{-6}	9.1189×10^{-9}
$S > 0$	2.7015×10^{-7}	2.7288×10^{-7}	6.8567×10^{-9}

Text S3: Influences of simplification bias

We examine whether the non-monotonic ε–$\bar{r}$ relationship suggested by Equation 9 is resulted from the approximations made during the equation derivation. With the probability density functions (PDFs) of r_0 and S_m written as $f(r_0)$ and $g(S_m)$, respectively, the original definitions of $\bar{r}$ and ε are

$$\bar{r} = \int\int r(S_m, r_0) f(r_0) g(S_m) \mathrm{d}S_m \, \mathrm{d}r_0 \quad , \text{(S1)}$$

$$\varepsilon^2 = \frac{1}{(\bar{r})^2}[r(S_m, r_0) - \bar{r}]^2 f(r_0) g(S_m) \mathrm{d}S_m \mathrm{d}r_0, \text{(S2)}$$

where $r(S_m, r_0)$ is calculated by Equation 5 in the Manuscript, with G set to 1.00×10^6 s cm^{-2} (Manton, 1979), and t set to 1200 s. We also discretize r_0 and S_m logarithmetically into 200 bins. The boundaries for r_0 are $r_{0,\min} = 1$μm and $r_{0,\max} = 32$ μm, and the boundaries for S_m are $S_{m,\min} = 0.0001$% and $S_{m,\max} = 10$%, respectively.

To calculate ε and $\bar{r}$ from their original definitions, we assume both $f(r_0)$ and $g(S_m)$ satisfy log-normal distributions:

$$f(r_0) = e^{-\frac{(\ln r_0 - \mu_1)^2}{2\lambda_1{}^2}} \Big/ \int_{r_{0,\min}}^{r_{0,\max}} e^{-\frac{(\ln r_0 - \mu_1)^2}{2\lambda_1{}^2}} \mathrm{d}r_0, \text{(S3)}$$

$$g(S_\mathrm{m}) = e^{-\frac{(\ln S_\mathrm{m} - \mu_2)^2}{2\lambda_2^2}} \Big/ \int_{S_{\mathrm{m,min}}}^{S_{\mathrm{m,max}}} e^{-\frac{(\ln S_\mathrm{m} - \mu_2)^2}{2\lambda_2^2}} \mathrm{d}S_\mathrm{m}. \text{(S4)}$$

To compare Figure S3 with Figure 4, μ_1 and λ_1 are set to 0.405 and 0.647, respectively, to ensure that ε_0 and $\overline{r_0}$ are the same as used in Figure 4. The values of μ_2 and λ_2 are varied within ranges -8 to 0 and 0.1 to 0.75, respectively, to cover the range of $\sigma_{S_\mathrm{m}}/\bar{S}_\mathrm{m}$ in Figure 4.

With these settings, ε is calculated by its original definition (Equation S2), showing good agreement with Figure 4a which is calculated from Equation 9. This means the non-monotonic ε–$\bar{r}$ relationship is a nature of the analytical model rather than our simplification bias. When explaining the ε–N_a relationships, we prefer to use the simplified form (Equation 9) instead of the original definition (Equation S2). The reason is that the original definition requires $f(r_0)$ and $g(S_m)$ which are more difficult to obtain compared to ε_0, $\bar{r_0}$, and $\sigma_{S_m}/\bar{S}_m$ needed by the simplified form, and also, the roles of r_0 and S_m are more clear in the simplified form than in the original definition.

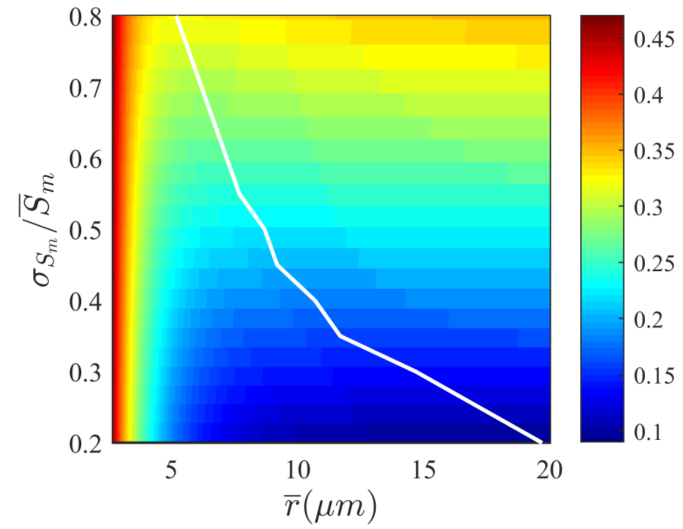

Figure S3. Assuming both droplet's time-averaged supersaturation (S_m) and droplet's initial radius (r_0) follow lognormal distribution, this figure illustrates the joint dependence of droplet spectral relative dispersion (ε) on droplet mean radius ($\bar{r}$) and relative dispersion of S_m (i.e., $\sigma_{S_m}/\bar{S}_m$). The white solid line marks the minimum point of ε.

Supporting Information References

Khain, A., Ovtchinnikov, M., Pinsky, M., Pokrovsky, A., & Krugliak, H. (2000). Notes on the state-of-the-art numerical modeling of cloud microphysics. *Atmospheric Research,* 55(3-4), 159-224. https://doi.org/10.1016/s0169-8095(00)00064-8

Manton, M. J. (1979). On the broadening of a droplet distribution by turbulence near cloud base. *Quarterly Journal of the Royal Meteorological Society*, 105(446), 899-914. https://doi.org/10.1002/qj.49710544613

Smagorinsky, J. (1963). General Circulation Experiments with the Primitive Equations: I. The Basic Experiment. *Monthly Weather Review*, 91(3), 99-164. https://doi.org/10.1175/1520-0493(1963)091<0099:GCEWTP>2.3.CO;2